The Journal of Infectious Diseases

SUPPLEMENT ARTICLE

A Fluorescently Labeled Marburg Virus Glycoprotein as a New Tool to Study Viral Transport and Assembly

Eva Mittler,[1,a] Gordian Schudt,[1,a] Sandro Halwe,[1,2,a] Cornelius Rohde,[1,2] and Stephan Becker[1,2]

[1]Institut für Virologie, Philipps-Universität Marburg, and [2]German Center of Infection Research, Partner Site Giessen-Marburg-Langen, Marburg, Germany

The single surface glycoprotein (GP) of filoviruses is indispensable for recognition of its cellular receptor and infection of target cells. To study the intracellular trafficking of GP by using live-cell imaging, the mucin-like domain of Marburg virus (MARV) GP was replaced by the fluorophore mCherry ($GP_{\Delta MLD\_mCherry}$). Intracellular distribution, surface transport, and recruitment of $GP_{\Delta MLD\_mCherry}$ into virus-like particles were similar to observations for wild-type GP. Using reverse genetics, we generated a recombinant MARV expressing $GP_{\Delta MLD\_mCherry}$ (recMARV $MARV_{GP\Delta MLD\_mCherry}$). Time-lapse microscopy of recMARV $MARV_{GP\Delta MLD\_mCherry}$–infected cells revealed that $GP_{\Delta MLD\_mCherry}$–positive vesicles were transported to the cell surface in a tubulin-dependent manner. Moreover, dual-color live-cell imaging revealed cotransport of $GP_{\Delta MLD\_mCherry}$ and VP40 and their colocalization at the plasma membrane. In this proof-of-concept study we showed that the newly developed $GP_{\Delta MLD\_mCherry}$ is a promising tool to elucidate intracellular trafficking and assembly pathways of MARV.

Keywords. Marburg virus; dual-color live-cell imaging; cytoskeleton; reverse genetic system; intracellular transport.

Marburg virus (MARV), a filovirus, is highly pathogenic for humans and nonhuman primates and, as a risk group 4 agent, is handled under biosafety level 4 (BSL-4) conditions [1]. Currently, no approved vaccines and antivirals are available for human use.

The current understanding of the assembly process of filoviral particles remains fragmentary [2, 3]. Early assembly steps occur in virus-induced perinuclear inclusion bodies, where the viral helical nucleocapsids are formed [4, 5]. Previous live-cell imaging studies of filovirus-infected cells revealed an actin-driven transport of nucleocapsids from inclusion bodies to the virus assembly sites at the plasma membrane, where budding and release of progeny virions take place [5–13].

The MARV glycoprotein (GP), a class I viral fusion protein, is composed of 2 subunits, GP_1 (170 kDa) and GP_2 (46 kDa), linked by disulfide bonds [14]. GP_1 comprises the receptor-binding domain, as well as numerous N- and O-glycosylation sites, with the O-glycosylation sites being concentrated in the mucin-like domain (MLD), spanning amino acids 289–501 [14, 15]. Previous reports have shown that the MLD is dispensable for efficient GP-mediated infection of target cells [16–19]. GP is translated at the rough endoplasmic reticulum and hijacks the secretory pathway, crossing the endoplasmic reticulum, Golgi apparatus, and trans-Golgi network to reach the plasma membrane, from where it is incorporated into the budding viral particles [20]. During transport, GP becomes acylated, O and N glycosylated, proteolytically cleaved into GP_1 and GP_2, and phosphorylated [20–23].

The filovirus matrix protein VP40 is a peripheral membrane protein with several functions in the viral replication cycle, which are partially regulated by its different oligomeric states. While dimerization of VP40 is essential for intracellular transport, hexamers of VP40 mediate budding of virus-like particles at the plasma membrane, and octamers of VP40 regulate viral transcription and replication [24–27]. VP40 is also essential for the assembly of filoviral particles; its phosphorylation triggers the interaction with nucleocapsids in the periphery of infected cells and their transport into filopodia, the sites of viral budding [7, 8, 10]. The intracellular trafficking of VP40 to the plasma membrane includes interaction with small transport vesicles and an association with late endosomes and multivesicular bodies, followed by the formation of VP40-enriched clusters in the periphery [9, 28]. Upon coexpression of GP and VP40, both proteins accumulate in VP40-induced peripheral clusters; this encounter is critical for the proper incorporation of GP into budding filamentous particles [12, 13, 29]. To date, the spatiotemporal dynamics of the formation of the viral envelope containing high amounts of GP and VP40 is not understood.

To examine viral envelope assembly by time-lapse microscopy, we constructed and characterized a fluorescently labeled GP in which the MLD was substituted by the fluorophore mCherry ($GP_{\Delta MLD\_mCherry}$). Using reverse genetics, we replaced the GP gene in the genome of MARV with $GP_{\Delta MLD\_mCherry}$ and subsequently rescued a recombinant MARV ($recMARV_{GP\Delta MLD\_mCherry}$). Here, we report that the generation of $recMARV_{GP\Delta MLD\_mCherry}$ allowed us to faithfully monitor GP's intracellular transport in a live-cell

Present affiliations: Department of Microbiology and Immunology, Albert Einstein College of Medicine, Bronx, New York (E. M.); and GSK Vaccines, Marburg, Germany (G. S.).

[a]E. M., G. S., and S. H. contributed equally to this report.

Correspondence: S. Becker, PhD, Institut für Virologie, Philipps-Universität Marburg Hans-Meerwein-Straße 2, 35043 Marburg, Germany (becker@staff.uni-marburg.de).

The Journal of Infectious Diseases® 2018;218(S5):S318–26

DOI: 10.1093/infdis/jiy424

setting. Moreover, using dual-color live-cell imaging, we also analyzed cotransport of the 2 major components of the filoviral envelope, $GP_{\Delta MLD\_mCherry}$ and GFP-VP40, in infected cells under BSL-4 conditions.

MATERIALS AND METHODS

Cell Lines and Viruses

Human embryonic kidney (HEK293) cells (American Type Culture Collection [ATCC], Manassas, VA), African green monkey kidney cells (Vero E6; ATCC) and human hepatoma cells (Huh-7; kindly provided by R. Bartenschlager, Heidelberg, Germany) were maintained in Dulbecco's modified Eagle's medium supplemented with 10% (v/v) fetal calf serum, 2 mM L-glutamine, 50 U/mL penicillin, and 50 µg/mL streptomycin (Gibco) at 37°C and 5% CO_2. During live-cell imaging experiments, Huh-7 cells were cultivated in Leibovitz's medium (Life Technologies) supplemented with 100 U/mL penicillin, 100 µg/mL streptomycin, 20% (v/v) fetal calf serum, and 400 µM 6-hydroxy-2,5,7,8-tetramethylchromane-2-carboxylic acid (Trolox, Sigma).

Rescue and propagation of recombinant MARV (recMARV) were achieved as described by Dolnik et al [6]. In short, Huh-7 and Vero E6 cells were mixed in a 1:1 proportion and subjected to transfection with support plasmids (encoding MARV nucleoprotein [NP], VP35, VP30, L, and T7 polymerase) and with the full-length complementary DNA construct of MARV Musoke (GenBank accession number NC001608), in which the open-reading frame (ORF) of MARV GP was exchanged to MARV $GP_{\Delta MLD\_mCherry}$ (also see the "Plasmids and Molecular Cloning" subsection, below). Culture supernatants were blind passaged onto Vero E6 cells 7 days after transfection. Western blot analysis of culture supernatants, using MARV-specific antibodies, and RNA isolation and sequencing were used to confirm recombinant virus rescue. Infections with recMARV were performed under BSL-4 conditions at the Institute of Virology, Philipps University (Marburg, Germany).

Plasmids and Molecular Cloning

Plasmids encoding MARV NP, VP35, VP30, L, VP24, VP40, and GP under the control of a chicken β-actin promoter (vector pCAGGS) were constructed as described in previous publications [13, 30, 31]. Plasmids coding for the MARV-specific minigenome (3M5M) and the T7 DNA-dependent RNA polymerase were described elsewhere [31, 32]. Generation of pCAGGS-MARV $GP_{\Delta MLD\_mCherry}$ was performed by amplifying sequences encoding amino acids 1–288 and amino acids 502–681 of MARV GP, as well as the ORF of the fluorophore mCherry by polymerase chain reaction (PCR). Primers introduced additional sequences for flexible glycine-serine linkers (GS_6) connecting the fluorescent protein with the C- and N-terminus of amplified fragments 1–288 and 502–681, respectively. Purified PCR products were linked via recombinant PCR and cloned into pCAGGS via the restriction enzymes SmaI and SacI. Cloning of full-length MARV complementary DNA was performed as described elsewhere [12]. Substitution of MARV GP by MARV $GP_{\Delta MLD\_mCherry}$ in the full-length MARV complementary DNA clone was performed using standard cloning techniques. For generation of the plasmid pCAGGS-MARV-GFP-VP40, the green fluorescent protein (GFP) ORF was cloned together with a GS_{12} linker in front of the VP40 ORF, using homologous recombination and primer-extension PCR [33, 34]. All constructs were verified by Sanger sequencing. Detailed cloning strategies, as well as primer sequences, are available on request.

50% Tissue Culture Infectious Dose ($TCID_{50}$) Assay

Infectivity of recMARV and $recMARV_{GP\Delta MLD\_mCherry}$ particles released into the cell supernatant was determined by a $TCID_{50}$ assay. Vero E6 cells were cultured in 96-well plates to 50% confluence and inoculated in quadruplicate with 10-fold serial dilutions of supernatants of infected Vero E6 cells. At 10 days after infection, assays were evaluated, and titers, measured in $TCID_{50}$/milliliter, were calculated using the Spearman-Kaerber method [35].

Infectious Virus-Like Particle (iVLP) Assay

The MARV iVLP assay was performed as described earlier [31].

Indirect Immunofluorescence (IF) Analysis

Huh-7 cells were transfected with plasmids encoding MARV proteins, using TransIT-LT1 (Mirus Bio). For coexpression of MARV VP40 and GP or $GP_{\Delta MLD\_mCherry}$, plasmids were used in a ratio of 4:1 to achieve a protein ratio similar to MARV-infected cells [13]. Permeabilization of cells and blocking of nonspecific signals was performed as described previously [9]. Antibodies were diluted in blocking buffer: monoclonal mouse anti-GP immunoglobulin (diluted 1:50; targets receptor-binding domain [amino acids 38–188], Fig. S1) and polyclonal rabbit anti-GP serum (1:50), as well as monoclonal mouse anti-VP40 antibody (1:50). All secondary anti-mouse or anti-rabbit antibodies conjugated to Alexa Fluor 488, Alexa Fluor 555, or Alexa Fluor 647 (Life Technologies) were diluted 1:400. Microscopic analyses were performed at 63 times the original magnification with an Axiomat fluorescence microscope (Zeiss) and a confocal laser scanning microscope (Leica SP5), respectively. In the case of native IF analysis, staining was performed as described previously [13].

Electrophoresis and Western Blot Analysis

Sodium dodecyl sulfate (SDS) gel electrophoresis (10%) and subsequent Western blot analysis were performed as described recently [9]. Antibodies were diluted in PBS_{def} containing 0.1% Tween and 1% milk powder. Mouse monoclonal antibodies were used for detection of MARV GP (1:100), NP (1:200), and VP40 (1:200) followed by goat anti-mouse antibody conjugated with horseradish peroxidase (HRP; Dako) as secondary

antibody. Quantification of protein bands was performed using the Image Lab software of the Bio-Rad Laboratories Chemidoc System (Bio-Rad).

Treatment of Cells with Cytoskeleton-Modulating Drugs

Cells were transfected and treated at 4 hours after transfection with 15 μM nocodazole (Sigma), 0.3 μM cytochalasin D (Sigma), or 0.15% dimethyl sulfoxide (DMSO [vehicle] Sigma). In case of live-cell experiments chemicals were added to the cell culture medium 24 hours after infection and 3 hours before fluorescence microscopy was performed. Control cells were only treated with 0.15% DMSO.

Live-Cell Microscopy

For live-cell imaging, Huh-7 cells were seeded into 35-mm μ-dishes (Ibidi) 24 hours prior to infection. Cells were infected with recMARV or recMARV$_{GP\Delta MLD_mCherry}$ with a multiplicity of infection of 1 $TCID_{50}$ per cell in 400 μL of Opti-MEM (Life Technologies) for 1 hour. The inoculum was then removed, and, if needed, cells were transfected in a 1000-μL final volume of CO_2-independent Leibovitz's medium (Life Technologies). Live-cell time-lapse experiments were recorded with a Leica DMI6000B, using an oil objective (63 times the original magnification) equipped with a remote control device to operate the microscope from outside the BSL-4 facility. Pictures and movie sequences were processed with Leica LAS AF software package and Nikon NIS Elements 3.1, respectively.

RESULTS AND DISCUSSION

Construction, Imaging, and Tracking of MARV GP Labeled With mCherry

Monitoring the intracellular transport of GP in real time is necessary to understand the spatiotemporal dynamics of the surface protein and its interaction with viral and cellular proteins. To this end, we labeled GP with an intrinsic monomeric red fluorophore, mCherry. To avoid interference of the bulky fluorophore with GP's vital functions during virus entry, assembly and budding, mCherry needed to be embedded into the GP domain structure [36]. However, pilot experiments showed that simply fusing mCherry to the cytoplasmic domain of GP strongly affected transport (data not shown). Since previous studies suggested that the MLD of MARV GP was dispensable for virus entry and infection of cultured cells [17, 37], we replaced the MLD by mCherry (GP$_{\Delta MLD_mCherry}$; Figure 1A). This procedure removed the furin cleavage site C-terminal of amino acid 435 which was described to be expendable for replication of Ebola virus in cell culture [38, 39]. To confirm functional integrity of GP$_{\Delta MLD_mCherry}$, human hepatoma cells (Huh-7) were transfected with a plasmid encoding GP$_{\Delta MLD_mCherry}$ and subjected to IF analysis and live-cell imaging at 24 hours after transfection (Figure 1B–D). GP$_{\Delta MLD_mCherry}$ showed a vesicular staining pattern similar to wild-type GP which was in agreement with localization of the proteins in the secretory pathway including the endoplasmic reticulum and Golgi apparatus (Figure 1B) [13, 20]. In addition, GP$_{\Delta MLD_mCherry}$ and GP accumulated in a punctate pattern at the plasma membrane (Figure 1B). The fluorescent signals of the immunolabeled GP$_{\Delta MLD_mCherry}$ (green) and its considerably weaker red auto-fluorescence overlapped almost completely indicating mCherry being tightly associated with GP. Time-lapse imaging revealed transport of vesicles harboring GP$_{\Delta MLD_mCherry}$ within the cell body with a mean velocity (±SD) of 1629 ± 573 nm/second (n = 30; Figure 1C), which was suggestive of tubulin-driven transport [40].

To further address the interplay between GP$_{\Delta MLD_mCherry}$–positive vesicles and the cytoskeleton, we analyzed the influence of cytoskeleton-modulating drugs on the intracellular distribution of GP$_{\Delta MLD_mCherry}$ (Figure 1D). To assess the efficiency of GP's transport to the plasma membrane, surface GP was stained in nonpermeabilized cells, using an antibody against GP and a fluorescently tagged secondary antibody (Figure 1D). Cells were pretreated with either nocodazole, an inhibitor of microtubule polymerization, or cytochalasin D, which inhibits actin assembly, while in the control setting only the vehicle (DMSO) was added. Treatment of cells with nocodazole or cytochalasin D led to the expected destruction of cellular actin or tubulin cytoskeleton, respectively, while both remained intact in control cells (Supplementary Figure 2). In DMSO-treated control cells expressing GP$_{\Delta MLD_mCherry}$, we observed a relatively weak intracellular signal and distinct surface staining of GP$_{\Delta MLD_mCherry}$. After nocodazole treatment, cells presented a strong accumulation of GP$_{\Delta MLD_mCherry}$ in the perinuclear area accompanied by a decrease of GP$_{\Delta MLD_mCherry}$ localized at the cell surface (Figure 1D). This phenotype points to a disrupted trafficking of GP$_{\Delta MLD_mCherry}$ from the perinuclear area to the cell periphery in the absence of a functional tubulin network. In contrast, cytochalasin D–treated cells exhibited surface expression levels of GP$_{\Delta MLD_mCherry}$ similar to those of control cells. The intracellular signal of GP$_{\Delta MLD_mCherry}$ in cytochalasin D–treated cells was increased in comparison to control cells but distributed more homogenously. Moreover, formation of GP$_{\Delta MLD_mCherry}$–positive protrusions at the plasma membrane was reduced (Figure 1D), which is consistent with the reported key role of actin in formation of filopodia. The stronger GP signal in the cell periphery was probably caused by the disrupted actin cortex beneath the plasma membrane, which might have prevented efficient release of surface-bound GP into the supernatant [41]. We have shown before that release of filamentous VP40-induced VLPs is influenced by actin polymerization [10]. Although some of the GP signal overlapped with the nucleus, Z stacks of GP-expressing cells clearly showed that the nucleus is free of GP (Supplementary Figure 3 and Supplementary Video 1). Therefore, the GP$_{\Delta MLD_mCherry}$ signal is most likely located above or below the nucleus, which could not be differentiated with the chosen settings of the microscope (ie, a full open pinhole).

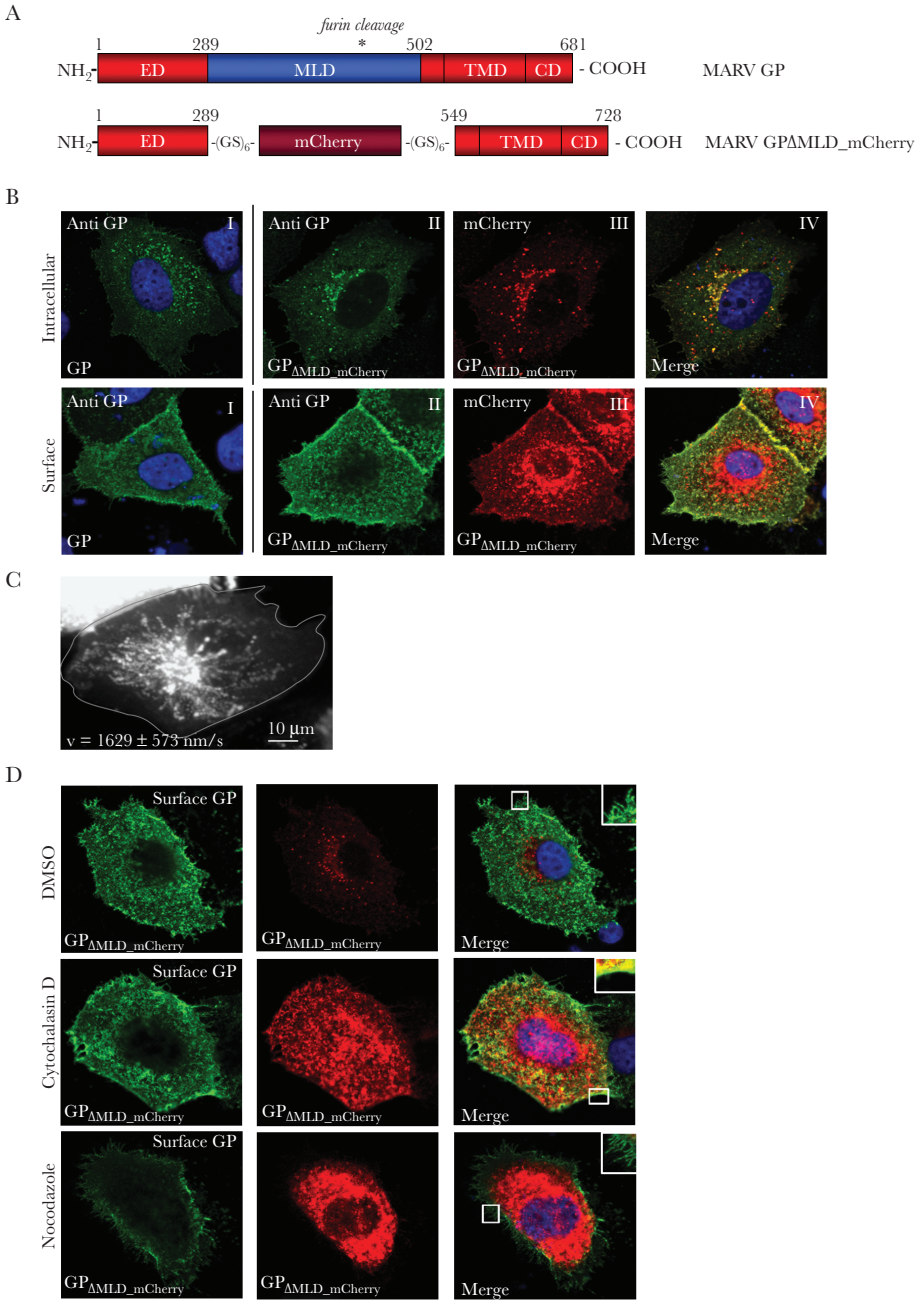

Figure 1. An intrinsic fluorophore allows imaging and tracking of Marburg virus (MARV) glycoprotein (GP). *A*, Schematic model of MARV $GP_{\Delta MLD\_mCherry}$ fusion protein. Filoviral GPs are composed of the N-terminal ectodomain (ED), the hydrophobic membrane-spanning transmembrane domain (TMD), and the C-terminal cytoplasmic domain (CD). The chimera of MARV GP in which the mucin-like domain (MLD) was substituted with the fluorochrome mCherry is designated MARV $GP\Delta_{MLD\_mCherry}$. The asterisk indicates the furin cleavage site C-terminal of amino acid 435. *B*, To determine the intracellular distribution of MARV $GP\Delta_{MLD\_mCherry}$, subconfluent Huh-7 cells were transfected with plasmids encoding MARV GP (left) or MARV $GP\Delta_{MLD\_mCherry}$ (right). For intracellular staining, cells were fixed 24 hours after transfection with 4% paraformaldehyde and subjected to immunofluorescence using a monoclonal mouse anti-MARV GP immunoglobulin G (IgG) targeting the receptor-binding domain; bound antibodies were detected with an Alexa Fluor 488–labeled goat anti-mouse IgG serum. Nuclei were counterstained with DAPI. To evaluate surface distribution of MARV $GP\Delta_{MLD\_mCherry}$ by surface staining, cells were fixed but not permeabilized (note the difference from cells shown in upper panel) and stained with a monoclonal mouse anti-MARV GP IgG at 4°C for 1 hour. Bound antibodies were detected using a goat anti-mouse IgG serum conjugated with Alexa Fluor 647, respectively. Nuclei were counterstained with DAPI. *C*, To determine the velocity (*v*) of MARV $GP\Delta_{MLD\_mCherry}$ vesicles, Huh-7 cells transiently expressing MARV $GP\Delta_{MLD\_mCherry}$ were analyzed by time-lapse microscopy 24 hours after transfection. Shown is the representative maximal intensity projection of 57 single frames, corresponding to 4 minutes. The time between each frame is 4.2 seconds. Vesicles (n = 30) were analyzed and tracked. *D*, Nocodazole treatment inhibits transport of $GP\Delta_{MLD\_mCherry}$ to the cell periphery. Subconfluent Huh-7 cells were transfected with plasmids encoding MARV $GP\Delta_{MLD\_mCherry}$ and treated with dimethyl sulfoxide (DMSO), cytochalasin D (0.3 µM), or nocodazole (15 µM) 4 hours after transfection. At 24 hours after transfection, surface GP was stained with a monoclonal mouse anti-MARV GP IgG at 4°C for 1 hour, fixation with 4% paraformaldehyde (no permeabilization) was performed, and bound antibodies were detected using a goat anti-mouse IgG serum conjugated with Alexa Fluor 647. Nuclei were counterstained with DAPI. Framed areas in the right column show cellular protrusions and are displayed enlarged in the upper right area of each panel.Images were acquired using a confocal laser scanning microscope (Leica). In case of images including surface-stained GP image acquisition was performed with a maximally open pinhole.

In summary, these results support the idea that trafficking of $GP_{\Delta MLD\_mCherry}$–positive vesicles proceeds from the perinuclear area to the cell surface in a tubulin-dependent manner. In addition, as the bulky mCherry did not impair intracellular transport of $GP_{\Delta MLD\_mCherry}$, the generated fluorescently labeled GP represents a versatile tool to monitor the intracellular fate of the MARV GP.

MARV $GP\Delta_{MLD\_mCherry}$ Is Fully Functional in Mediating Infection of Target Cells

GP is the only MARV surface protein and is essential for recognizing the cellular receptor NPC1 and for mediating fusion of the viral membrane with cellular membranes to release the nucleocapsid into the cytoplasm of the target cell [16, 17]. Proper incorporation of GP into the viral membrane is accomplished by sorting GP into plasma membrane compartments enriched with the viral matrix protein VP40. VP40 orchestrates most of the viral assembly steps and mediates budding of MARV [8, 9, 13]. Colocalization analyses were performed in Huh-7 cells expressing $GP_{\Delta MLD\_mCherry}$ and VP40, which revealed that the 2 proteins colocalized in peripheral clusters similar to wild-type GP and VP40 (Figure 2A) [10]. Using an iVLP assay, we next analyzed whether $GP_{\Delta MLD\_mCherry}$ was efficiently incorporated into budding particles [31, 42]. The iVLP assay is based on the expression of all MARV proteins and a MARV-specific minigenome. The minigenome is replicated and encapsidated to form mininucleocapsids, which are transported to the plasma membrane and released by budding from the cell surface [31, 42]. Budding takes place at sites where VP40 and GP are available in high concentrations, resulting in the release of iVLPs [10]. In this setting, GP was replaced by $GP_{\Delta MLD\_mCherry}$, and the transfected cells, as well as the purified released iVLPs, were analyzed by Western blot. $GP_{\Delta MLD\_mCherry}$ was highly expressed in the transfected cells (Figure 2B), and release of $GP_{\Delta MLD\_mCherry}$-containing iVLPs was detected although reduced in comparison with GP-containing iVLPs (Figure 2B). We also observed that GP supported VP40's function to mediate particle budding, confirming previously published data [43] (Figure 2B). However, $GP_{\Delta MLD\_mCherry}$ did not seem to increase budding of iVLPs induced by VP40 (Figure 2B).

iVLPs released from either GP- or $GP_{\Delta MLD\_mCherry}$–expressing cells were purified from the supernatant of the producer cells and quantified by Western blot analysis using antibodies targeting the NP. Equal amounts of iVLPs normalized to NP were used to infect Huh-7 cells, which had been pretransfected with plasmids encoding L, NP, VP35, and VP30 to support transcription and replication of the incoming minigenomes [31]. Resulting *Renilla* luciferase activity in the target cells served to monitor GP- or $GP_{\Delta MLD\_mCherry}$–mediated infection. Measured luciferase activity was not significantly different in cells infected by either of the 2 different iVLPs, suggesting that $GP_{\Delta MLD\_mCherry}$ had a similar ability to mediate receptor recognition and fusion as its wild-type counterpart (Figure 2C). This is consistent with previous reports showing that the receptor-binding site of GP (amino acids 38–188) is only exposed and available for binding to the cellular receptor NPC1 after considerable parts of the protein, including the MLD (or mCherry in $GP_{\Delta MLD\_mCherry}$), have been removed by endo/lysosomal cysteine-dependent proteases [44, 45].

Rescue and Characterization of Recombinant $MARV_{GP\Delta MLD\_mCherry}$

To investigate the function of $GP_{\Delta MLD\_mCherry}$ in MARV-infected cells, we replaced the ORF of GP by the gene encoding $GP_{\Delta MLD\_mCherry}$ in a plasmid containing the full-length MARV genome [46]. The resulting plasmid was used to rescue recombinant MARV ($recMARV_{GP\Delta MLD\_mCherry}$), and its phenotype was characterized in comparison to recMARV (Figure 3) [17]. Growth kinetics of the 2 viruses were analyzed by infecting African green monkey kidney cells (Vero E6) at a multiplicity of infection of 0.01. Virus replication was monitored by Western blot analyses of cell lysates and supernatants, as well as by determining the titer of released viruses through $TCID_{50}$ assays. Both $recMARV_{GP\Delta MLD\_mCherry}$ and recMARV replicated efficiently, allowing the detection of viral proteins in Vero E6 cell lysates starting from days 3–4 after infection (for NP) or day 7 after infection (for VP40). The growth of $recMARV_{GP\Delta MLD\_mCherry}$ was slightly accelerated, with NP being detectable already at day 3 after infection. Released viral proteins were detected by Western blot at day 7 after infection (Figure 3A). This result was confirmed by $TCID_{50}$ assays of virus particles released into the supernatant of infected cells (Figure 3B). While $recMARV_{GP\Delta MLD\_mCherry}$ seemed to grow faster and to slightly higher titers than recMARV, the difference was not statistically significant (Figure 3B). Interestingly, the apparent inhibitory effect of $GP_{\Delta MLD\_mCherry}$, which led to a reduction of VLP release in the iVLP system, was not observed for $recMARV_{GP\Delta MLD\_mCherry}$. While the iVLP assay was performed in HEK293 cells, recombinant MARV was rescued and titered by using Vero E6 cells, suggesting that cell-line-specific differences are involved in the phenotype of $GP_{\Delta MLD\_mCherry}$.

In summary, our results indicate that fluorescently labeled $recMARV_{GP\Delta MLD\_mCherry}$ replicates efficiently in cell culture and displays growth kinetics similar to those of recMARV decorated with wild-type GP. Hence, we suggest that $recMARV_{GP\Delta MLD\_mCherry}$ faithfully mimics essential aspects of MARV particle entry, replication, and assembly.

Dual-Color Live-Cell Imaging of $recMARV_{GP\Delta MLD\_mCherry}$–Infected Cells

As Huh-7 cells are much flatter than Vero E6 cells and thus are better suited for live-cell imaging, the intracellular transport of $GP_{\Delta MLD\_mCherry}$ and virus envelope assembly were analyzed in $recMARV_{GP\Delta MLD\_mCherry}$–infected Huh-7 cells. Time-lapse microscopy was performed 19 hours after infection, which allowed the observation of fluorescent protein trafficking in cells that predominantly underwent the first MARV replication cycle (approximately 16 hours). Migrating MARV nucleocapsids

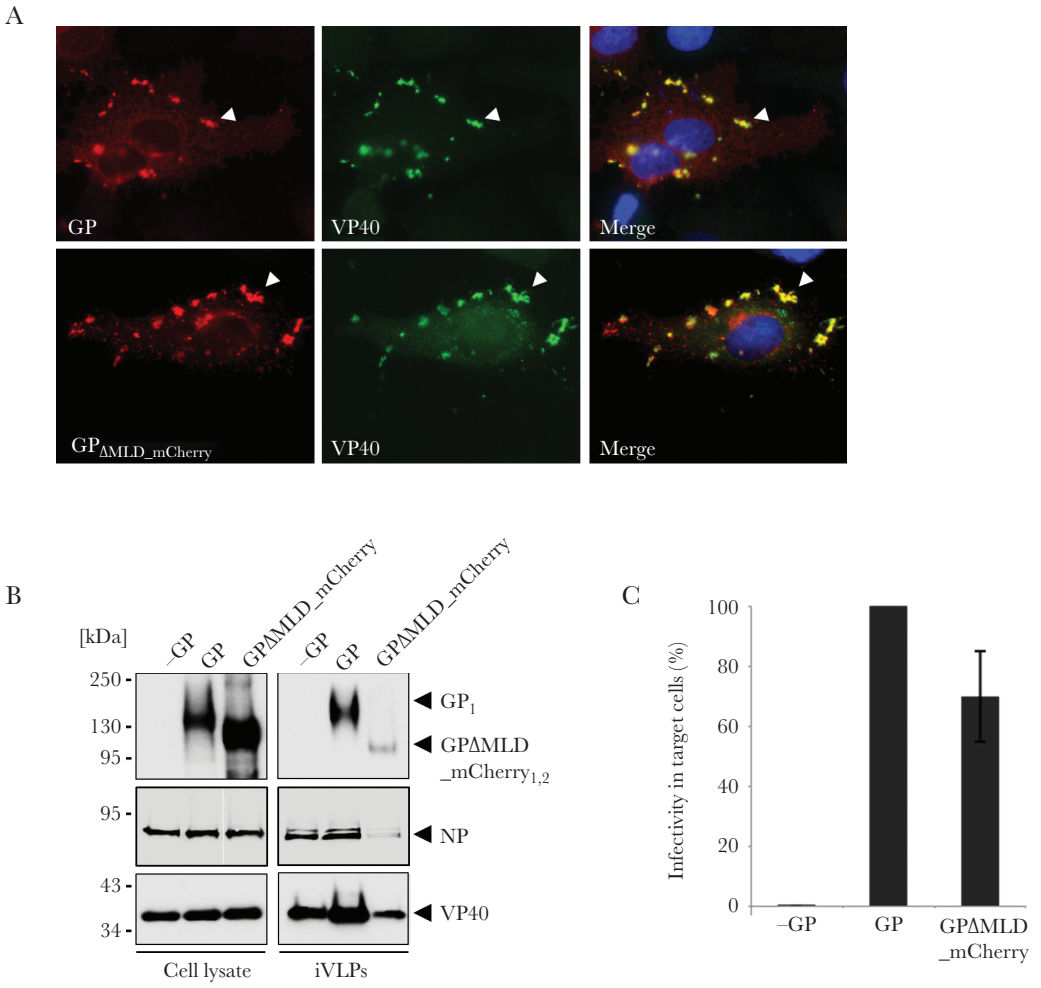

Figure 2. Fluorescently labeled Marburg virus (MARV) glycoprotein (GP) is fully functional in mediating infection of target cells. *A*, Colocalization of $GP_{\Delta MLD\_mCherry}$ with VP40. Huh-7 cells were cotransfected with plasmids encoding MARV VP40 and GP or $GP_{\Delta MLD\_mCherry}$. At 24 hours after transfection, cells were fixed and immunostained with a mouse anti-MARV VP40 monoclonal antibody and a rabbit anti-MARV GP immunoglobulin G (IgG). As secondary antibodies, a goat anti-mouse IgG conjugated with Alexa Fluor 488 and a goat anti-rabbit conjugated with Alexa Fluor 555 were used. Arrowheads indicate colocalization of VP40 and GP or $GP_{\Delta MLD\_mCherry}$ in peripheral clusters. Images were acquired using an Axiomat fluorescence microscope (Zeiss). *B*, Incorporation of $GP_{\Delta MLD\_mCherry}$ into infectious virus-like particles (iVLPs). HEK293 cells were transfected with plasmids carrying a MARV-specific minigenome containing the *Renilla* luciferase reporter gene and with plasmids encoding the T7 DNA-dependent RNA polymerase and all structural MARV proteins, including MARV GP or MARV $GP\Delta_{MLD\_mCherry}$. At 60 hours after transfection, particulate material in the cellular supernatant was pelleted through a 20% sucrose cushion. Purified iVLPs and lysed cells were subjected to sodium dodecyl sulfate gel electrophoresis and blotted onto a nitrocellulose membrane. Immunostaining was performed with monoclonal mouse anti-MARV GP, anti-MARV VP40, or anti-MARV nucleoprotein (NP) IgGs, followed by incubation with a secondary horseradish peroxidase (HRP)–coupled anti-mouse antibody. *C*, Infectivity of iVLPs incorporating MARV $GP_{\Delta MLD\_mCherry}$. Purified iVLPs were used to infect target cells that had been pretransfected with plasmids encoding MARV NP, VP35, VP30, and L. Cells were harvested 60 hours after infection, and cell lysates were assayed for *Renilla* luciferase reporter gene activity. Data represent mean values ± standard deviations for 8 independent experiments.

resulting from secondary infection of neighboring cells cannot be detected at this time point. $GP_{\Delta MLD\_mCherry}$–positive vesicles displayed varying transport directionalities, with an average velocity (±SD) of 1569 ± 397 nm/second for vesicles moving to the cell center and 1941 ± 515 nm/second for vesicles moving to the cell periphery; centrifugal and centripedal vesicle transport were not significantly different. Statistical analyses also revealed that the velocity of $GP_{\Delta MLD\_mCherry}$–positive vesicles in infected cells was comparable to the velocity of $GP_{\Delta MLD\_mCherry}$–positive vesicles in transfected cells (mean [±SD], 1629 ± 573 nm/seconds). We also analyzed the transport of $GP_{\Delta MLD\_mCherry}$–bearing vesicles in the presence of the cytoskeleton-disrupting agents nocodazole and cytochalasin D. Maximum intensity projections of time-lapse imaging revealed that, during nocodazole treatment, transport of $GP_{\Delta MLD\_mCherry}$–positive vesicles was abolished, which manifested in dot-like protein accumulations (Figure 4A). In contrast, concluding from the observed trajectories, cytochalasin D had no influence on the transport kinetics of GP vesicles (Figure 4A). Hence, the movement of $GP_{\Delta MLD\_mCherry}$–positive vesicles was clearly dependent on the polymerization of tubulin but not actin. Moreover, in addition to their susceptibility to nocodazole, the speed of $GP_{\Delta MLD\_mCherry}$–positive vesicles also supported the

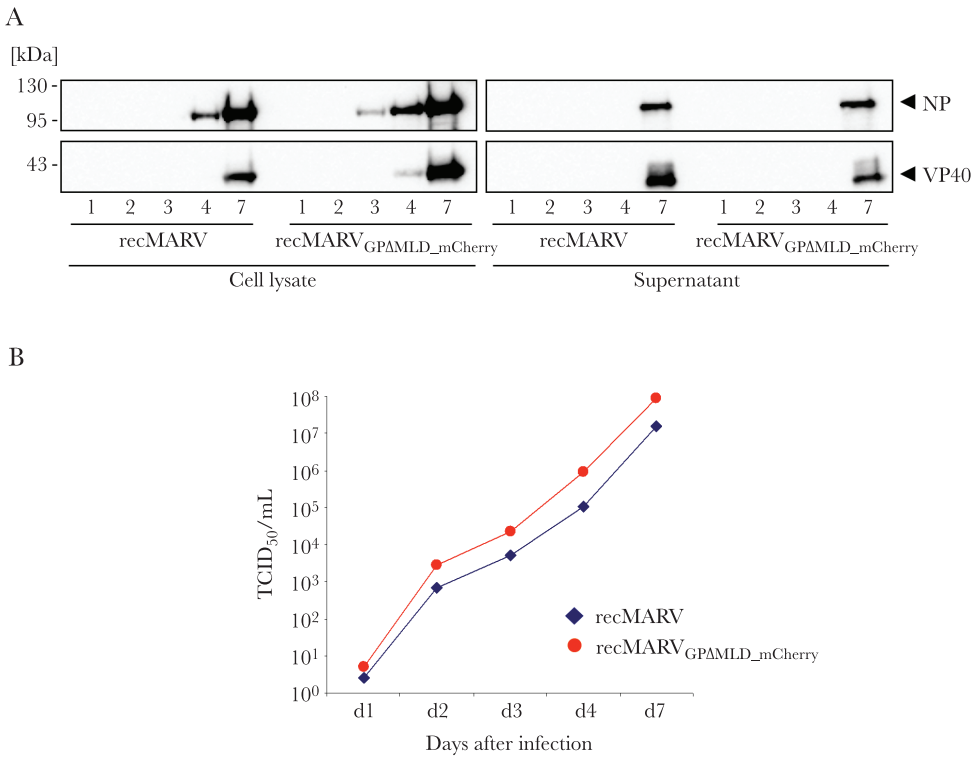

Figure 3. Recovery and characterization of the chimera of Marburg virus (MARV) glycoprotein (GP) in which the mucin-like domain (MLD) was substituted with the fluorochrome mCherry (MARV GP$\Delta_{MLD_mCherry}$). *A*, recMARV$_{GP\Delta MLD_mCherry}$ is released in similar quantities as wild-type recombinant MARV (recMARV). Vero E6 cells were infected with recMARV or recMARV$_{GP\Delta MLD_mCherry}$ at a multiplicity of infection of 0.01 50% tissue culture infective doses (TCID$_{50}$). At the indicated time points, cell lysates and cell culture supernatants were collected, inactivated, and subjected to quantitative Western blot analyses. Immunostaining was performed with a mouse monoclonal anti-MARV nucleoprotein (NP) or anti-MARV VP40 immunoglobulin G (IgG), and bound antibodies were detected by incubation with a secondary horseradish peroxidase–coupled anti-mouse antibody (upper panel). *B*, recMARV$_{GP\Delta MLD_mCherry}$ and wild-type recMARV grow to comparable virus titers. Cell culture supernatants from the growth kinetics analysis were collected, and the infectious titers were determined via the TCID$_{50}$ assay. Data represent the mean values of 2 independent experiments (lower panel).

assumption of a tubulin-dependent transport [40]. These findings are in line with published data describing cell surface–directed transport of GP through the secretory pathway and, as such, through a trafficking route separate from the viral nucleocapsids [2, 7, 8, 20]. Usurpation of the tubulin cytoskeleton as a means to transport viral components has been detected for viruses such as Lassa virus, adenovirus, pseudorabiesvirus, and herpes simplex virus 1 [47–50].

At present, the section of the secretory pathway that filoviral GPs are hijacking to facilitate transport to the site of virus budding is not completely understood. Previous studies revealed VP40-mediated recruitment of GP to peripheral VP40-positive structures, which is consistent with the essential function of VP40 for budding and assembly of MARV [13, 29]. It was unclear, however, whether GP and VP40 are cotransported to the plasma membrane or reach the plasma membrane independently. Here, we used infection by recMARV$_{GP\Delta MLD_mCherry}$ in combination with ectopic expression of GFP-tagged VP40 to further define (co-)distribution and (co-)transport of both proteins. A similar approach was already successfully implemented in a previous study published by our laboratory that focused on the function of VP40 in MARV nucleocapsid transport [8]. Snapshots of time-lapse imaging studies indicated colocalization of GP$_{\Delta MLD_mCherry}$ and GFP-VP40 in the perinuclear region (Figure 4B). In addition, vesicles were observed that were positive for either one or both of the proteins GP$_{\Delta MLD_mCherry}$ or GFP-VP40 (Figure 4B). As exemplarily shown using maximal intensity projection, GFP-VP40 and GP$_{\Delta MLD_mCherry}$ were cotrafficked over a distance of several µm with a velocity of 1200 ± 446 nm/second in the periphery of infected cells (Figure 4B). During a 30-minute time-lapse interval, we observed GP and VP40 appearing simultaneously at the cell margins, where both proteins colocalized and were especially enriched in delicate filamentous protrusions of approximately 1 µm in length (Figure 4C). Our results indicate that GP and VP40 cover sections of their intracellular transport routes separately. In the cell periphery, however, the transport trajectories of both proteins intersect, ultimately resulting in formation of GP- and VP40-positive protrusions at the cell margins. Based on our data, we also hypothesize that the observed GP- and VP40-enriched plasma membrane domains represent precursors for the assembly of MARV envelopes.

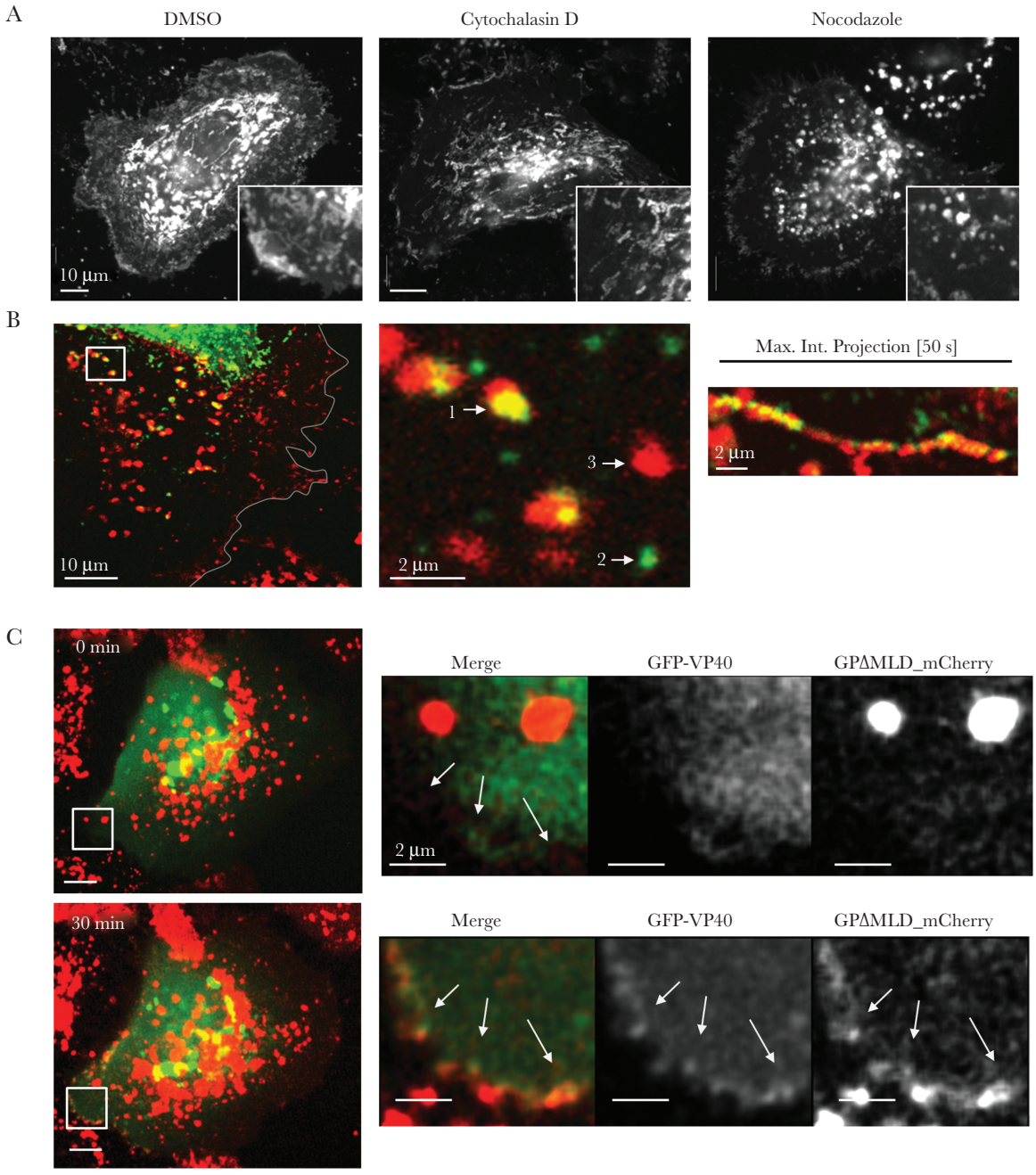

Figure 4. Use of the chimera of Marburg virus (MARV) glycoprotein (GP) in which the mucin-like domain (MLD) was substituted with the fluorochrome mCherry (MARV $GP\Delta_{MLD\_mCherry}$) as a tool for tracking intracellular vesicle transport. *A*, Nocodazole treatment inhibits transport of $GP_{\Delta MLD\_mCherry}$ whereas cytochalasin D treatment does not. Huh-7 cells infected with $recMARV_{GP\Delta MLD\_mCherry}$ at a multiplicity of infection of 1 were incubated with cytochalasin D (0.3 µM) or nocodazole (15 µM), respectively, for 3 hours at 19 hours after infection. Intracellular vesicle movement was monitored by time-lapse live-cell imaging and displayed as representative maximal intensity projection of 50 frames, corresponding 50 seconds. Enlarged cellular areas are displayed in the lower right corner. *B*, Cotransport of MARV $GP_{\Delta MLD\_mCherry}$ and GFP-VP40 in infected cells. Huh-7 cells were infected with $recMARV_{GP\Delta MLD\_mCherry}$, followed by transfection with a plasmid encoding GFP-VP40 1 hour after infection. At 19 hours after infection, cells were analyzed by time-lapse microscopy. The framed area in the left panel is enlarged in the middle panel, showing (1) vesicular colocalization of $GP_{\Delta MLD\_mCherry}$ and GFP-VP40, (2) a GFP-VP40–positive vesicle, and (3) a $GP_{\Delta MLD\_mCherry}$–positive vesicle. GFP-VP40 and $GP_{\Delta MLD\_mCherry}$ were cotransported over several micrometers, shown in a maximal intensity projection of 50 seconds (right). *C*, $GP_{\Delta MLD\_mCherry}$ and GFP-VP40 reach the plasma membrane simultaneously. Time-lapse microscopy of cells treated like those in panel B was performed 22 hours after infection, with a frame taken every 2 minutes. Framed areas in left panels represent marginal cell areas and are enlarged in the right panels. Elapsed time between upper frames and lower frames was 30 minutes.

Taken together, our initial proof-of-concept study describes $recMARV_{GP\Delta MLD\_mCherry}$ as a novel, versatile tool to perform in-depth analyses of the assembly of the viral envelope. Further work is needed and will focus on providing a more comprehensive understanding of the spatiotemporal dynamics of virus progeny formation.

Supplementary Data

Supplementary materials are available at *The Journal of Infectious Diseases* online. Consisting of data provided by the authors to benefit the reader, the posted materials are not copyedited and are the sole responsibility of the authors, so questions or comments should be addressed to the corresponding author.

Notes

Acknowledgments. We thank Astrid Herwig, Katharina Kowalski, and Dirk Becker, for excellent technical assistance; Dr Markus Eickmann, for supervision; and Gotthard Ludwig and Michael Schmidt, for technical support of BSL-4 work.

Financial support. This work was supported by the Jürgen-Manchot-Stiftung (to S. H. and C. R.) and by the Deutsche Forschungsgemeinschaft, through the Collaborative Research Centers SFB 593 and SFB 1021.

Potential conflicts of interest. All authors: No reported conflicts of interest. All authors have submitted the ICMJE Form for Disclosure of Potential Conflicts of Interest. Conflicts that the editors consider relevant to the content of the manuscript have been disclosed.

References

1. Rougeron V, Feldmann H, Grard G, Becker S, Leroy EM. Ebola and Marburg haemorrhagic fever. J Clin Virol **2015**; 64:111–9.
2. Nanbo A, Watanabe S, Halfmann P, Kawaoka Y. The spatio-temporal distribution dynamics of Ebola virus proteins and RNA in infected cells. Sci Rep **2013**; 3:1206.
3. Welsch S, Kolesnikova L, Krähling V, Riches JD, Becker S, Briggs JA. Electron tomography reveals the steps in Filovirus budding. PLoS Pathog **2010**; 6:e1000875.
4. Dolnik O, Stevermann L, Kolesnikova L, Becker S. Marburg virus inclusions: a virus-induced microcompartment and interface to multivesicular bodies and the late endosomal compartment. Eur J Cell Biol **2015**; 94:323–31.
5. Hoenen T, Shabman RS, Groseth A, et al. Inclusion bodies are a site of Ebolavirus replication. J Virol **2012**; 86:11779–88.
6. Dolnik O, Kolesnikova L, Welsch S, Strecker T, Schudt G, Becker S. Interaction with Tsg101 is necessary for the efficient transport and release of nucleocapsids in marburg virus-infected cells. PLoS Pathog **2014**; 10:e1004463.
7. Schudt G, Dolnik O, Kolesnikova L, Biedenkopf N, Herwig A, Becker S. Transport of Ebolavirus nucleocapsids is dependent on actin polymerization: live-cell imaging analysis of Ebolavirus-infected cells. J Infect Dis **2015**; 212(Suppl 2):S160–6.
8. Schudt G, Kolesnikova L, Dolnik O, Sodeik B, Becker S. Live-cell imaging of Marburg virus-infected cells uncovers actin-dependent transport of nucleocapsids over long distances. Proc Nat Acad Sci U S A **2013**; 110:14402–7.
9. Kolesnikova L, Berghöfer B, Bamberg S, Becker S. Multivesicular bodies as a platform for formation of the Marburg virus envelope. J Virol **2004**; 78:12277–87.
10. Kolesnikova L, Bohil AB, Cheney RE, Becker S. Budding of Marburgvirus is associated with filopodia. Cell Microbiol **2007**; 9:939–51.
11. Kolesnikova L, Mittler E, Schudt G, Shams-Eldin H, Becker S. Phosphorylation of Marburg virus matrix protein VP40 triggers assembly of nucleocapsids with the viral envelope at the plasma membrane. Cell Microbiol **2012**; 14:182–97.
12. Mittler E, Kolesnikova L, Herwig A, Dolnik O, Becker S. Assembly of the Marburg virus envelope. Cell Microbiol **2013**; 15:270–84.
13. Mittler E, Kolesnikova L, Strecker T, Garten W, Becker S. Role of the transmembrane domain of Marburg virus surface protein GP in assembly of the viral envelope. J Virol **2007**; 81:3942–8.
14. Feldmann H, Will C, Schikore M, Slenczka W, Klenk HD. Glycosylation and oligomerization of the spike protein of Marburg virus. Virology **1991**; 182:353–6.
15. Geyer H, Will C, Feldmann H, Klenk HD, Geyer R. Carbohydrate structure of Marburg virus glycoprotein. Glycobiology **1992**; 2:299–312.
16. Carette JE, Raaben M, Wong AC, et al. Ebola virus entry requires the cholesterol transporter Niemann-Pick C1. Nature **2011**; 477:340–3.
17. Mittler E, Kolesnikova L, Hartlieb B, Davey R, Becker S. The cytoplasmic domain of Marburg virus GP modulates early steps of viral infection. J Virol **2011**; 85:8188–96.
18. Ou W, Delisle J, Jacques J, et al. Induction of ebolavirus cross-species immunity using retrovirus-like particles bearing the Ebola virus glycoprotein lacking the mucin-like domain. Virol J **2012**; 9:32.
19. Tran EE, Simmons JA, Bartesaghi A, et al. Spatial localization of the Ebola virus glycoprotein mucin-like domain determined by cryo-electron tomography. J Virol **2014**; 88:10958–62.
20. Becker S, Klenk HD, Mühlberger E. Intracellular transport and processing of the Marburg virus surface protein in vertebrate and insect cells. Virology **1996**; 225:145–55.
21. Funke C, Becker S, Dartsch H, Klenk HD, Mühlberger E. Acylation of the Marburg virus glycoprotein. Virology **1995**; 208:289–97.
22. Sänger C, Mühlberger E, Ryabchikova E, Kolesnikova L, Klenk HD, Becker S. Sorting of Marburg virus surface protein and virus release take place at opposite surfaces of infected polarized epithelial cells. J Virol **2001**; 75:1274–83.
23. Volchkov VE, Volchkova VA, Ströher U, et al. Proteolytic processing of Marburg virus glycoprotein. Virology **2000**; 268:1–6.
24. Bornholdt ZA, Noda T, Abelson DM, et al. Structural rearrangement of Ebola virus VP40 begets multiple functions in the virus life cycle. Cell **2013**; 154:763–74.
25. Gomis-Ruth FX, Dessen A, Timmins J, et al. The matrix protein VP40 from Ebola virus octamerizes into pore-like structures with specific RNA binding properties. Structure **2003**; 11:423–33.
26. Hoenen T, Biedenkopf N, Zielecki F, et al. Oligomerization of Ebola virus VP40 is essential for particle morphogenesis and regulation of viral transcription. J Virol **2010**; 84:7053–63.
27. Hoenen T, Volchkov V, Kolesnikova L, et al. VP40 octamers are essential for Ebola virus replication. J Virol **2005**; 79:1898–905.
28. Kolesnikova L, Bugany H, Klenk HD, Becker S. VP40, the matrix protein of Marburg virus, is associated with membranes of the late endosomal compartment. J Virol **2002**; 76:1825–38.
29. Kolesnikova L, Ryabchikova E, Shestopalov A, Becker S. Basolateral budding of Marburg virus: VP40 retargets viral glycoprotein GP to the basolateral surface. J Infect Dis **2007**; 196(Suppl 2):S232–6.
30. Bamberg S, Kolesnikova L, Möller P, Klenk HD, Becker S. VP24 of Marburg virus influences formation of infectious particles. J Virol **2005**; 79:13421–33.
31. Wenigenrath J, Kolesnikova L, Hoenen T, Mittler E, Becker S. Establishment and application of an infectious virus-like particle system for Marburg virus. J Gen Virol **2010**; 91:1325–34.
32. Mühlberger E, Weik M, Volchkov VE, Klenk HD, Becker S. Comparison of the transcription and replication strategies of marburg virus and Ebola virus by using artificial replication systems. J Virol **1999**; 73:2333–42.
33. Hawkins NC, Garriga G, Beh CT. Creating precise GFP fusions in plasmids using yeast homologous recombination. Biotechniques **2003**; 34:74–8, 80.
34. Higuchi R, Krummel B, Saiki RK. A general method of in vitro preparation and specific mutagenesis of DNA fragments: study of protein and DNA interactions. Nucleic Acids Res **1988**; 16:7351–67.
35. Hierholzer JC, Killington RA. Virus isolation and quantitation. Virology Methods Manual **1996**:36–8.
36. Hashiguchi T, Fusco ML, Bornholdt ZA, et al. Structural basis for Marburg virus neutralization by a cross-reactive human antibody. Cell **2015**; 160:904–12.
37. Manicassamy B, Wang J, Rumschlag E, et al. Characterization of Marburg virus glycoprotein in viral entry. Virology **2007**; 358:79–88.
38. Neumann G, Feldmann H, Watanabe S, Lukashevich I, Kawaoka Y. Reverse genetics demonstrates that proteolytic processing of the Ebola virus glycoprotein is not essential for replication in cell culture. J Virol **2002**; 76:406–10.
39. Volchkov VE, Feldmann H, Volchkova VA, Klenk HD. Processing of the Ebola virus glycoprotein by the proprotein convertase furin. Proceedings of the National Academy of Sciences of the United States of America **1998**; 95:5762–7.
40. Trinczek B, Ebneth A, Mandelkow EM, Mandelkow E. Tau regulates the attachment/detachment but not the speed of motors in microtubule-dependent transport of single vesicles and organelles. J Cell Sci **1999**; 112 (Pt 14):2355–67.
41. Arakawa Y, Cordeiro JV, Schleich S, Newsome TP, Way M. The release of vaccinia virus from infected cells requires RhoA-mDia modulation of cortical actin. Cell Host Microbe **2007**; 1:227–40.
42. Takamatsu Y, Kolesnikova L, Becker S. Ebola virus proteins NP, VP35, and VP24 are essential and sufficient to mediate nucleocapsid transport. Proc Natl Acad Sci U S A **2018**; 115:1075–80.
43. Radoshitzky SR, Dong L, Chi X, et al. Infectious Lassa virus, but not filoviruses, is restricted by BST-2/tetherin. J Virol **2010**; 84:10569–80.
44. Chandran K, Sullivan NJ, Felbor U, Whelan SP, Cunningham JM. Endosomal proteolysis of the Ebola virus glycoprotein is necessary for infection. Science **2005**; 308:1643–5.
45. Kuhn JH, Radoshitzky SR, Guth AC, et al. Conserved receptor-binding domains of Lake Victoria marburgvirus and Zaire ebolavirus bind a common receptor. J Biol Chem **2006**; 281:15951–8.
46. Krähling V, Dolnik O, Kolesnikova L, et al. Establishment of fruit bat cells (Rousettus aegyptiacus) as a model system for the investigation of filoviral infection. PLoS Negl Trop Dis **2010**; 4:e802.
47. Bosse JB, Bauerfeind R, Popilka L, et al. A beta-herpesvirus with fluorescent capsids to study transport in living cells. PLoS One **2012**; 7:e40585.
48. Fehling SK, Noda T, Maisner A, et al. The microtubule motor protein KIF13A is involved in intracellular trafficking of the Lassa virus matrix protein Z. Cell Microbiol **2013**; 15:315–34.
49. Forest T, Barnard S, Baines JD. Active intranuclear movement of herpesvirus capsids. Nat Cell Biol **2005**; 7:429–31.
50. Wisner TW, Sugimoto K, Howard PW, Kawaguchi Y, Johnson DC. Anterograde transport of herpes simplex virus capsids in neurons by both separate and married mechanisms. J Virol **2011**; 85:5919–28.